Article

Aerosol Effective Radiative Forcing in the Online Aerosol Coupled CAS-FGOALS-f3-L Climate Model

Hao Wang [1,2,3]**, Tie Dai** [1,2,*] **, Min Zhao** [1,2,3]**, Daisuke Goto** [4]**, Qing Bao** [1]**,
Toshihiko Takemura** [5] **, Teruyuki Nakajima** [4] **and Guangyu Shi** [1,2,3]

[1] State Key Laboratory of Numerical Modeling for Atmospheric Sciences and Geophysical Fluid Dynamics, Institute of Atmospheric Physics, Chinese Academy of Sciences, Beijing 100029, China; wanghao@lasg.iap.ac.cn (H.W.); zhaomin@lasg.iap.ac.cn (M.Z.); baoqing@lasg.iap.ac.cn (Q.B.); shigy@mail.iap.ac.cn (G.S.)

[2] Collaborative Innovation Center on Forecast and Evaluation of Meteorological Disasters/Key Laboratory of Meteorological Disaster of Ministry of Education, Nanjing University of Information Science and Technology, Nanjing 210044, China

[3] College of Earth and Planetary Sciences, University of Chinese Academy of Sciences, Beijing 100029, China

[4] National Institute for Environmental Studies, Tsukuba 305-8506, Japan; goto.daisuke@nies.go.jp (D.G.); nakajima.teruyuki@nies.go.jp (T.N.)

[5] Research Institute for Applied Mechanics, Kyushu University, Fukuoka 819-0395, Japan; toshi@riam.kyushu-u.ac.jp

* Correspondence: daitie@mail.iap.ac.cn; Tel.: +86-10-8299-5452

check for updates

Abstract: The effective radiative forcing (ERF) of anthropogenic aerosol can be more representative of the eventual climate response than other radiative forcing. We incorporate aerosol–cloud interaction into the Chinese Academy of Sciences Flexible Global Ocean–Atmosphere–Land System (CAS-FGOALS-f3-L) by coupling an existing aerosol module named the Spectral Radiation Transport Model for Aerosol Species (SPRINTARS) and quantified the ERF and its primary components (i.e., effective radiative forcing of aerosol-radiation interactions (ERFari) and aerosol-cloud interactions (ERFaci)) based on the protocol of current Coupled Model Intercomparison Project phase 6 (CMIP6). The spatial distribution of the shortwave ERFari and ERFaci in CAS-FGOALS-f3-L are comparable with that of most available CMIP6 models. The global mean 2014–1850 shortwave ERFari in CAS-FGOALS-f3-L (-0.27 W m^{-2}) is close to the multi-model means in 4 available models (-0.29 W m^{-2}), whereas the assessing shortwave ERFaci (-1.04 W m^{-2}) and shortwave ERF (-1.36 W m^{-2}) are slightly stronger than the multi-model means, illustrating that the CAS-FGOALS-f3-L can reproduce the aerosol radiation effect reasonably well. However, significant diversity exists in the ERF, especially in the dominated component ERFaci, implying that the uncertainty is still large.

Keywords: global climate model; anthropogenic aerosols; aerosol-radiation interaction; aerosol-cloud interaction; effective radiative forcing

1. Introduction

Aerosols impact the global climate by changing the Earth's radiation budget, which can not only scatter and absorb solar radiation directly [1], but also modify the cloud macro and micro physical properties by serving as the cloud condensation nuclei (CCN) and ice nuclei (IN) to indirectly perturb the Earth's radiation budget [2,3]. In addition, absorbing aerosols deposited on the ice and snow surface can also change the albedo of the Earth's surface [4]. Due to these comprehensive aerosol effects, there exist complex non-liner mechanisms, leading to the aerosol particles influencing radiative

forcing, especially aerosol–cloud interaction, which are still one of the largest uncertainties in the global climate projection [1,5,6].

The effective radiative forcing (ERF) of anthropogenic aerosols, defined as the change of net radiation flux at the top of atmosphere (TOA) with the same prescribed SSTs and sea ice but different aerosol emissions, is often used to quantify the radiative effects of aerosols [5,7]. Taking into account some rapid adjustments (i.e., atmospheric temperature, cloudiness, and water vapor), ERF can be more representative of the eventual temperature response than instantaneous radiative forcing [7,8].

The important tools available to investigate the ERF are the global climate model (GCM) and the Earth system model (ESM), which can be online coupled with global aerosol and chemical transport models. However, a large diversity still exists in the models; for example, the global mean ERF of anthropogenic aerosols assessed in the fifth assessment report of the Intergovernmental Panel on Climate Change (IPCC AR5) is -0.9 W m^{-2}, with a range from -1.9 to -0.1 W m^{-2} [5,6], which may partly due to the uncertainty of aerosol emissions in the pre-industrial era [9]. In addition, the longwave ERF ($+0.2$ W m^{-2}) in AR5 is based on expert judgement, whereas Heyn et al. 2017 [10] found that the ERF in the terrestrial spectrum may be smaller based on the models in the Coupled Model Intercomparison Project phase 5 (CMIP5). The ERF is also recommended to diagnose in the Aerosol Chemistry Model Intercomparison Project (AerChemMIP) and the Radiative Forcing Model Intercomparison (RFMIP), which are endorsed by the current CMIP6 and designed to quantify the climate impacts of aerosols [7,8,11].

The Chinese Academy of Sciences (CAS) Flexible Global Ocean–Atmosphere–Land System (FGOALS-f3-L) model developed by the State Key Laboratory of Numerical Modeling for Atmospheric Sciences and Geophysical Fluid Dynamics (LASG), Institute of Atmospheric Physics (IAP), CAS [12–14], has continuously contributed to the CMIP (including the current CMIP6) and the IPCC assessment reports [15]. A significant advantage is that the CAS FGOALS-f3-L can perform a higher resolution simulation (~25 km) using a finite volume dynamic core on the cubed-sphere grid [16,17]. However, the CAS-FGOALS-f3-L only includes the direct aerosols radiation effect offline by reading the prescribed three-dimension monthly aerosols concentration taken from the National Center for Atmospheric Research (NCAR) CAM-Chem model [18] and lacks the interactions between aerosols and cloud, leading to the aerosol not really matching the modelled meteorological fields, and we fail to investigate the climate effects of aerosols, such as assessing the ERF of anthropogenic aerosols. Recently, an existing aerosol module named the Spectral Radiation Transport Model for Aerosol Species (SPRINTARS; [19–22]) was successfully online coupled in the CAS FGOALS-f3-L, and the simulated spatial-temporal distributions of the Aerosol Optical Depths (AODs) has been evaluated with the multi-source satellites retrievals, which found that the SPRINTARS can reasonably reproduce the distribution of aerosol [23].

The main objective of this study is to further assess the effective radiation forcing (ERF) of anthropogenic aerosols with the new coupled model according to the current CMIP6 protocol and evaluate the performance of the model by comparing the ERF with the available results from CMIP6 models, which provides an important reference to study aerosol climate effect with the new coupled system in the future.

The paper is organized as follows. In Section 2, we describe the newly developed aerosol online coupled model and the methods to assess the ERF of anthropogenic aerosols. In Section 3, the aerosol–radiation interactions, aerosol–cloud interactions, and the effective radiation forcing of anthropogenic aerosols produced by the new coupled model are analyzed, respectively. We further discuss the overall model results in Section 4 and summarize the main findings in Section 5.

2. Model and Method

2.1. Model Description

The Chinese Academy of Sciences (CAS) Flexible Global Ocean–Atmosphere–Land System model (FGOALS-f3-L) is developed by the State Key Laboratory of Numerical Modeling for Atmospheric Sciences and Geophysical Fluid Dynamics (LASG), Institute of Atmospheric Physics (IAP), Chinese Academy of Sciences (CAS). Version 2 of the Finite-volume Atmospheric Model (FAMIL2; [13–15]) is the latest generation atmospheric component. A significant improvement is that its dynamical core uses a finite volume on a cubed-sphere grid [16,17] by replacing the previous Spectral Atmosphere Model (SAMIL; [24–26]), which leads to the horizontal resolution increasing from a minimum of number of 40 grid cells (C48, about 200 km) to a maximum of number of 1536 grid cells (C1536, about 6.25 km) [27,28]. Other improvements include introducing a new nonlocal high-order closure turbulence parameterization scheme [29] and a new Rapid Radiative Transfer Model for GCMs (RRTMG) with the correlated-k approach [30]. The mass mixing ratio of six hydrometeor species (i.e., water vapor, cloud water, cloud ice, rain, snow, and graupel) can be explicitly treated in the FAMIL2 [31–33]. As the scheme of diagnosing the cloud fractions considers both relative humidity and cloud mixing ratio [34], the cloud fractions diagnosed can be more precise. Other components, such as a land model and a sea ice model, are adopted for the Community Land Model (CLM4; [35]) and the Los Alamos sea ice model (CICE4; [36]), respectively.

The aerosol module called the Spectral Radiation Transport Model for Aerosol Species (SPRINTARS; [19–22,37]) was recently coupled in the CAS FGOALS-f3-L. It can treat the main tropospheric aerosol components (i.e., soil dust, sea salt, sulfate, and carbonaceous aerosols) and the precursor gases of sulfate. The SPRINTARS includes the main aerosol processes, such as emission, advection, convection, diffusion, sulfur chemistry, wet deposition, dry deposition, and gravitational settling. The mass mixing ratios are prognosed in every model time step, and the number of concentrations are diagnosed with the prognosed mass mixing ratios and the pre-prescribed particle size (dry mode radius and standard deviations) of each species in every model time step. Briefly, the dust and sea salt aerosol are divided by radius into 10 bins and 4 bins from 0.1 μm to 10 μm, whereas the sulfate and carbonaceous aerosol (including black carbon (BC), pure organic carbon (OC), internal mixture OC and BC (OC/BC)) are assumed to be monomodally lognormal size distributions with dry modal radii of 0.0695, 0.0118, 0.02, and 0.1 μm, respectively. Further details on the aerosol module can be found in the work of Takemura et al. [19,20,22] and Dai et al. [38,39]. The emission of the dust and sea salt are driven online by the 10 m wind speed at surface in every model time step [22,39]. A large difference is that the newer CMIP6 emission sources are updated in this study. In other words, the emission sources of carbonaceous aerosols, such as anthropogenic black carbon source (ANTBC), biomass burning black carbon source (BBBC), anthropogenic organic carbon source (ANTOC), biomass burning organic carbon source (BBOC), and the emissions sources of the anthropogenic sulfur dioxide source (ANTSO$_2$) and biomass burning sulfur dioxide source (BBSO$_2$), are all from the Community Emissions Data System (CEDS; [40,41]) for CMIP6. The ARG (Abdul-Razzak and Ghan; [42]) activation scheme, considering particle size, aerosol chemical component, and updraft velocity, is used in the model for water stratus clouds [20]. The berry-type autoconversion scheme [43], which includes the cloud condensation nuclei (CCN) effect, is adopted in the model, and the parameterization formula is the same as that used in [44].

2.2. Method

In this study, we focus on assessing the effective radiation forcing (ERF) of anthropogenic aerosols. According to the calculation method of Ghan, 2013 [45], the shortwave effective radiative forcing (ERF_{SW}) can be decomposed as follows:

$$ERF_{SW} = ERFari + ERFaci + \Delta SRE_{SW} \qquad (1)$$

where Δ is the difference between present day and preindustrial day, *ERFari* is the shortwave effective radiative forcing (ERF) of aerosol-radiation interactions (ari) or the shortwave direct radiative forcing, *ERFaci* is the shortwave effective radiative forcing (ERF) of aerosol-cloud interactions (aci) or the shortwave cloud radiative forcing under clean sky condition, and ΔSRE_{SW} is the surface albedo radiative forcing. The three components are further calculated as follows:

$$ERF_{SW} = \Delta F \tag{2}$$

$$ERFari = \Delta(F - F_{clean}) \tag{3}$$

$$ERFaci = \Delta\left(F_{clean} - F_{clean,clear}\right) \tag{4}$$

$$\Delta SRE_{SW} = \Delta\left(F_{clean,clear}\right) \tag{5}$$

where F is the net shortwave radiation flux at TOA, F_{clean} is the net shortwave flux at TOA under clean sky condition, $F_{clean,clear}$ is the net shortwave flux at TOA under clean clear sky condition. The diagnosis method of longwave effective radiative forcing (ERF_{LW}) is same as ERF_{SW}.

Following the simulation specification of AerChemMIP [11] and RFMIP [8], ERF is estimated using fixed SSTs and sea ice simulations, which are provided by the model's own preindustrial climatology data. Present day and preindustrial day refer to the years 2014 and 1850. Greenhouse gas concentrations are prescribed using 1850 climatology of CMIP6. The emissions of anthropogenic aerosols are taken from Hoesly et al. 2018 [40]. The only difference of two simulation experiments is the emission of anthropogenic aerosols. Each experiment is run for 30 years with the appropriate resolution of 200 km, and the annual means are used for analysis.

3. Results

We focus on assessing the effective radiative forcing of anthropogenic aerosol, which includes two main components, namely the ERFari and ERFaci. Before the discussion of each component, we first analysis the context related to the corresponding forcing component for a better understanding of how aerosols impact the climate system, such as the sulfate and carbonaceous aerosol optical depth, which related to the ERF_{ari}, and the cloud micro and macro physics properties, which related to the ERF_{aci}.

3.1. Aerosol–Radiation Interactions

3.1.1. Aerosol Optical Depth

Aerosols can scatter and absorb solar radiation directly. The aerosol optical depth (AOD) is an important aerosol optical property to measure how aerosols extinct the solar radiation in an atmospheric column.

Figure 1 shows the comparison of spatial distribution of the modelled annual average AOD in sulfate and carbonaceous aerosol between the years 2014 and 1850. Obviously, the sulfate and carbonaceous AOD increased significantly in the year 2014 relative to the year 1850, which can be attributed to the large emissions of anthropogenic aerosols (e.g., BC, OC) and sulfate precursor (e.g., SO_2). The high values of sulfate AOD (>0.2) are mainly located in East Asia, South Asia, South Africa, and their downwind direction in the year 2014 (Figure 1a), corresponding to the areas with the strong increased sulfate AOD (Figure 1c). The high values (>0.2) of carbonaceous AOD can be mainly found in East Asia, South Asia, Central Africa and their downwind direction in the year 2014 (Figure 1d), and East Asia and South Asia contribute the most in the increased carbonaceous AOD (Figure 1f). For the natural aerosols (i.e., dust and sea salt), their distributions of AOD values change little (not show), whereas the dust global mean AOD decreases about 2% in the year 2014. This very weak decrease is also found in the Grandey et al. 2018 [46], which may be due in part to there is relatively little change in the surface temperature with the fixed SSTs, so there would not be expected to be much of a change in dust emission [47]. In sum, the total AOD (global mean, 0.111) in the year 2014

increases about 39% (0.031) relative to the year 1850 (global mean, 0.08). The sulfate AOD contributes to about 71% (0.022), and the carbonaceous AOD contributes to the remainder 29% (0.009) (Figure 1c,f,i). The increased species AOD concentrates most in the Northern Hemisphere (NH), especially in East Asia and South Asia.
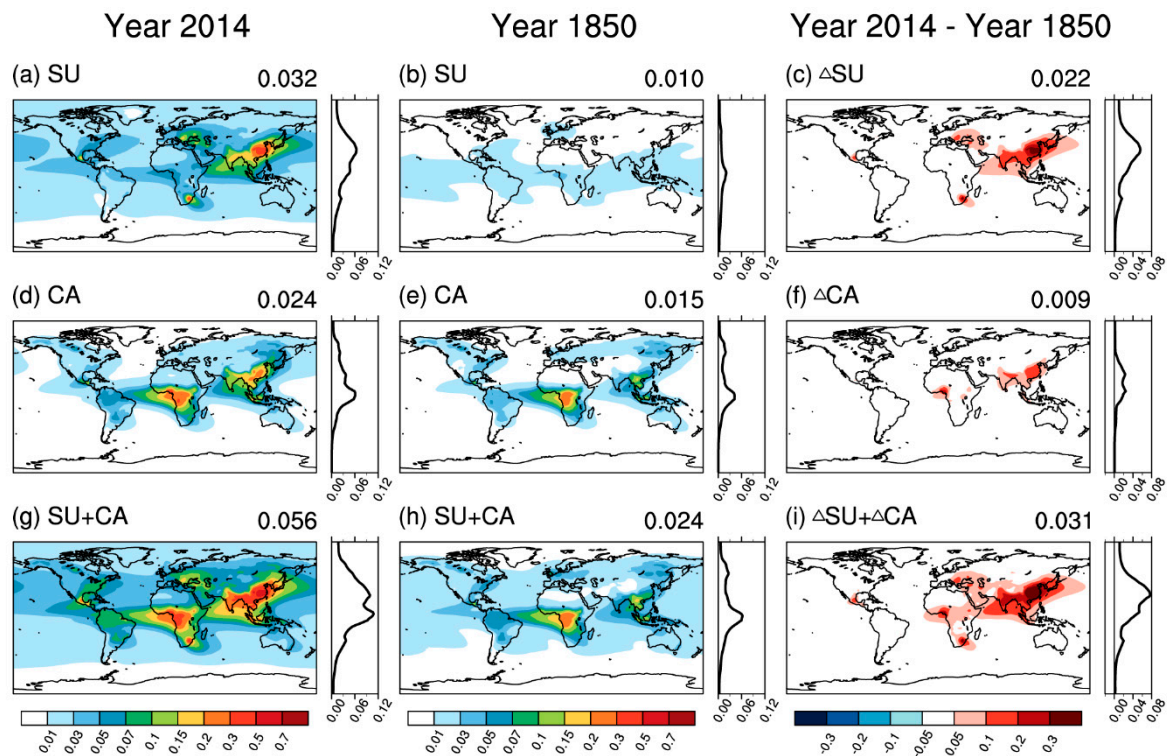

Figure 1. The first row is the modelled annual mean sulfate aerosol optical depth (AOD) in the year 2014 (**a**), the year 1850 (**b**), and the difference between the years 2014 and 1850 (**c**). The zonal means plot is located in the right of each subplot. The global mean value is shown the top right corner of each map, the second row (**d**–**f**) is same as the first row but for carbonaceous AOD (including pure black carbon and pure organic carbon, internal mixture black carbon and organic carbon), and the third row (**g**–**i**) is same as the first row but for the sum of sulfate and carbonaceous aerosols AOD. SU = sulfate, CA = carbonaceous aerosol, △= the AOD difference between the years 2014 and 1850.

3.1.2. Aerosol–Radiation Interactions

Figure 2 shows the comparison of shortwave direct radiative forcing between CAS-FGOALS-f3-L and other 5 CMIP6 model results (All defined model abbreviations are summarized in Table 1 note). As can be seen, the global distributions of shortwave ERFari in CAS-FGOALS-f3-L (This study) are closely relative to distribution of the 2014–1850 increased AOD (Figure 1i), as expected. It is noted that the absorbing aerosols (i.e., BC) exert the "warming effect", leading to a positive shortwave ERFari, which can partly offset the "cooling effect" of scattering aerosols (i.e., sulfate and organic carbon aerosol). To understand ERFari differences, a comparison of single scatter albedo (SSA) assumed for anthropogenic aerosol might be interesting. However, due to lack of SSA in CMIP6 models, Figure S1 (only shows the changes of SSA in CAS-FGOALS-f3-L. A weak change of SSA in East Asia mainly caused by the offset of scattering aerosol and absorbing aerosol. Therefore, although the East Asia exists the strongest extinction (Figure 1i), the "cooling effect" seems not too strong in CAS-FGOALS-f3-L, even resulting in some models (i.e., GFDL-ESM4 and UKESM1-0-LL) including the "warming effect," namely positive direct radiative forcing. In general, the global distributions of shortwave ERFari in CAS-FGOALS-f3-L are consistent with that in other models, whereas the radiation cooling intensity of aerosols in East Asia (EA) and South Asia (SA) (CAS-FGOALS-f3-L, EA: −1.24 W m^{-2}; SA: −2.14 W m^{-2}) are both slightly weak relative to the model CNRM-CM6-1, CNRM-ESM2-1 and MRI-ESM2-0 (EA:

ranges from −4.66 W m^{-2} to −2.53 W m^{-2}; SA: ranges from −3.69 W m^{-2} to −3.26 W m^{-2}), and slightly strong relative to the model GFDL-ESM4 (EA: 2.84 W m^{-2}; SA: −0.52 W m^{-2}) except UKESM1-0-LL (EA: 0.78 W m^{-2}; SA: −2.38 W m^{-2}). The global mean values of shortwave ERFari are −0.27, −0.42, −0.22, 0.24, −0.32 and −0.20 W m^{-2} for CAS-FGOALS-f3-L, CNRM-CM6-1, CNRM-ESM2-1, GFDL-ESM4, MRI-ESM2-0, and UKESM1-0-LL respectively. The CNRM_CM6-1 lacks apparent aerosol absorption (strong cooling near continental sources), whereas in GFDL-ESM4, the aerosol absorption is too strong, which is possibly due to more elevated absorbing aerosol above the clouds. In addition, since the outlier is the GFDL-ESM4 with an unlikely strong positive absorption (Figure 2d), the value of its shortwave ERFari are removed in statistical calculations (Table 1). Therefore, the multi-model mean value from the other four CMIP6 models is −0.29 W m^{-2}, with a small standard deviation (0.1) (Table 1).

Table 1. Comparison of annual mean effective radiative forcing in this study and 16 available CMIP6 model results * (unit: W m^{-2}).

	SW				LW				NET			
	ERFari	ERFaci	ΔSRE	ERF	ERFari	ERFaci	ΔSRE	ERF	ERFari	ERFaci	ΔSRE	ERF
ACCESS-CM2				−1.39				0.30				−1.09
BCC-ESM1				−3.90				0.29				−3.61
CNRM-CM6-1	−0.42	−0.74	−0.08	−1.25	0.00	−0.05	0.14	0.09	−0.42	−0.79	0.06	−1.15
CNRM-ESM2-1	−0.22	−0.59	−0.01	−0.82	0.00	−0.02	0.09	0.08	−0.21	−0.61	0.08	−0.74
CanESM5				−0.83				−0.02				−0.85
EC-Earth3				−0.84				0.03				−0.80
GFDL-ESM4	0.24	−0.77	−0.05	−0.59	0.02	−0.15	0.02	−0.11	0.26	−0.92	−0.03	−0.70
GFDL_CM4				−0.80				0.07				−0.73
GISS-E2-1-G				−1.06				0.13				−0.93
HadGEM3-GC31-LL				−1.29				0.19				−1.10
IPSL-CM6A-LR				−0.60				0.01				−0.59
MIROC6				−1.61				0.60				−1.01
MRI-ESM2-0	−0.32	−2.45	0.05	−2.73	0.00	1.48	0.04	1.52	−0.32	−0.97	0.09	−1.20
UKESM1-0-LL	−0.20	−1.02	−0.06	−1.28	0.05	0.01	0.11	0.17	−0.15	−1.01	0.06	−1.10
NorESM2-LM	−2.82	1.37	0.04	−1.41	0.04	0.16	0.01	0.21	−2.79	1.52	0.05	−1.21
NorESM2-MM	−2.95	1.43	0.06	−1.46	0.03	0.06	0.10	0.20	−2.91	1.49	0.16	−1.26
AVERAGE	−0.29	−0.78	−0.03	−1.07	0.01	−0.05	0.08	0.12	−0.28	−0.83	0.05	−0.92
STDEV	0.10	0.18	0.05	0.31	0.03	0.07	0.05	0.17	0.12	0.17	0.05	0.19
This study	**−0.27**	**−1.04**	**−0.05**	**−1.36**	**0.05**	**−0.04**	**0.08**	**0.09**	**−0.22**	**−1.09**	**0.03**	**−1.27**

* Note. SW = shortwave, LW = longwave, NET = shortwave + longwave, ERFaci, ERFari, and ΔSRE represent effective radiative forcing of aerosol-radiation interactions, effective radiative forcing of aerosol-cloud interactions, and surface albedo radiative forcing, respectively. ERF represents the effective radiative forcing. The Australian Community Climate and Earth System Simulator coupled model version 2(ACCESS-CM2), the Beijing Climate Center Earth System Model version 1 (BCC-ESM1), the Centre National de Recherches Météorologiques climate model version 6 (CNRM-CM6-1), the second version of the Centre National de Recherches Météorologiques Earth system model (CNRM-ESM2-1), the Canadian Earth System Model version 5 (CanESM5), the European Centre Earth System Model version 3 (EC-Earth3), the Geophysical Fluid Dynamics Laboratory coupled Earth System Model version 4 (GFDL-ESM4), the Geophysical Fluid Dynamics Laboratory Coupled Physical Climate Model version 4 (GFDL_CM4), the Goddard Institute for Space Studies ModelE version 2 (GISS-E2-1-G), the Hadley Centre Model Climate Global version 3 (HadGEM3-GC31-LL), the Institut Pierre-Simon Laplace Climate Modelling Centre climate model Version 6A and LR for low resolution (IPSL-CM6A-LR), the sixth version of the Model for Interdisciplinary Research on Climate (MIROC6), the Meteorological Research Institute Earth System Model version 2.0 (MRI-ESM2.0), the United Kingdom Earth System Model version 1.0 (UKESM1-0-LL), the Norwegian Earth System Model version 2 (NorESM2), the two versions presented here (NorESM2-LM and NorESM2-MM) represent the different horizontal resolution of the atmosphere and land component (approximately 2º for LM and 1º in MM). AVERAGE and STDEV represent the multi-model means and standard deviation. The results in BCC-ESM1 are removed in statistical calculations due to its unlikely strong negative shortwave ERF; The results of ERFari and ERF in GFDL-ESM4 are removed in statistical calculations due to its unlikely strong positive shortwave ERFari; The results of ERFaci and ERF in MRI-ESM2-0 are removed due to its strong ERFari with added aerosol/ice-cloud interactions; Model NorESM2-LM and NorESM2-MM are also excluded in statistical calculations due to unreasonable results of ERFaci and ERFari. All available model results of CMIP6 are download from https://esgf-node.llnl.gov/search/cmip6/, and the calculation methods are same as Ghan et al. 2013 [45].
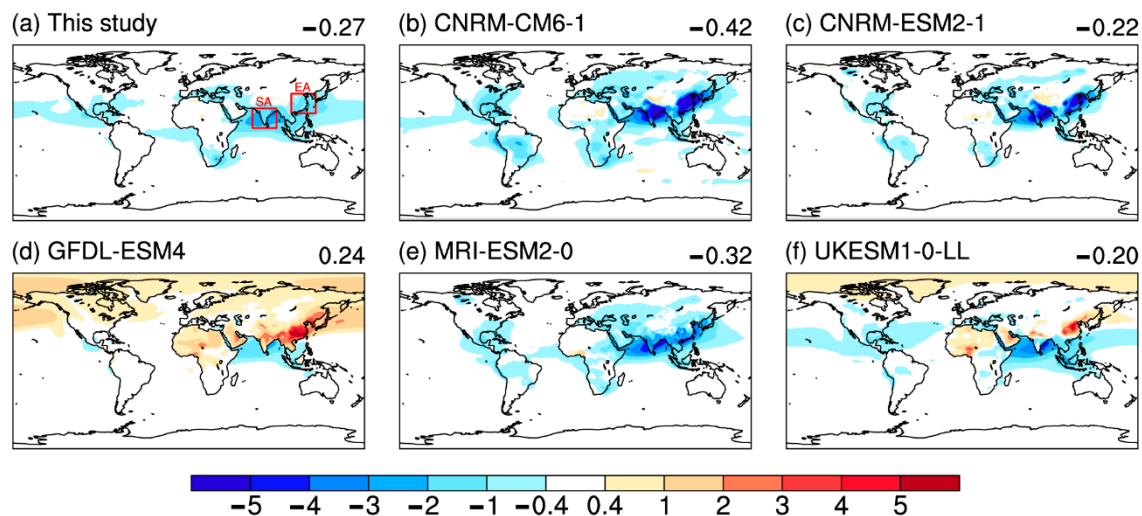
Shortwave ERFari (W m^{-2})

Figure 2. Comparison of annual mean shortwave effective radiative forcing of aerosol-radiation interactions in this study (**a**) and five available (**b**–**f**) Coupled Model Intercomparison Project phase 6 (CMIP6) model results.

3.2. Aerosol–Cloud Interactions

3.2.1. Cloud Physical Properties

Figure 3 shows the comparison of the main cloud micro and macro physical properties for the year 2014 and year 1850. The aerosol particles, especially the hydrophilic particles (e.g., sulfate, OC, sea salt), can act as the cloud condensation nuclei (CCN) to impact the cloud properties. Therefore, we first show the surface CCN number concentration at a fixed supersaturation of 0.1% to look at how much CCN changes in the year 2014 relative to the year 1850, although we notice that it is not necessarily a very good indicator to reveal the relevant CCN number concentration in the real atmosphere [48]. The locations of the large increase in CCN number concentration (Figure 3c) are similar with the increase of the sulfate and carbonaceous AOD (Figure 1i). The global mean surface CCN number concentration is 69.3 cm^{-3}, which is slightly lower than that of the result of 97.8 cm^{-3} from Liu et al. 2012 [49] using the modal aerosol module (MAM7). The value of percentage increase is 101% (Figure 3c), which is close to the result of 115% from Grandey et al. 2018 [46], although their value was taken from the level of 860 hPa. Figure 3d–f shows the distribution of the column-integrated cloud droplet number concentration (CDNC) for the year 2014, 1850, and the difference between the year 2014 and 1850. The spatial distributions of CDNC difference (Figure 3f) are similar to the pattern of AOD difference (Figure 1i), mainly due to the increase of sulfate and carbonaceous aerosol drive the increases of CDNC. The global mean cloud droplet effective radius at the cloud top above 273 K reduces from 9.9 μm to 9.2 μm (Figure 3g–i), which can be mainly attributed to the significant increases of CDNC when the cloud liquid water path (LWP) is assumed constant (i.e., Twomey effect), although the small increases exist in LWP (Figure 3l). Most of the decreased regions are located in the midlatitude of the Northern Hemisphere, especially in the regions emitting the anthropogenic aerosol heavily and their downwind direction. The weak increase of LWP (Figure 3l) is possibly caused by the decrease of precipitation rate (refers to the warm cloud precipitation, Figure S2, Supplementary Materials), which is related to the aerosol second indirect effect. Generally, an increase of the CDNC number concentration drives a decrease of precipitation rate, which are represented in the CAS-FGOALS-f3-L model using the Berry-type autoconversion scheme [43,44], although we note that the nonlinear CCN-precipitation mechanism may possibly more complicated in reality. In addition, cloud fraction (CF) has been shown

to have a potentially large impact on the ERFaci, a small increase in CF (0.2%, Figure 3o), especially in the low CF (0.3%, Figure S3i) are found in our model.
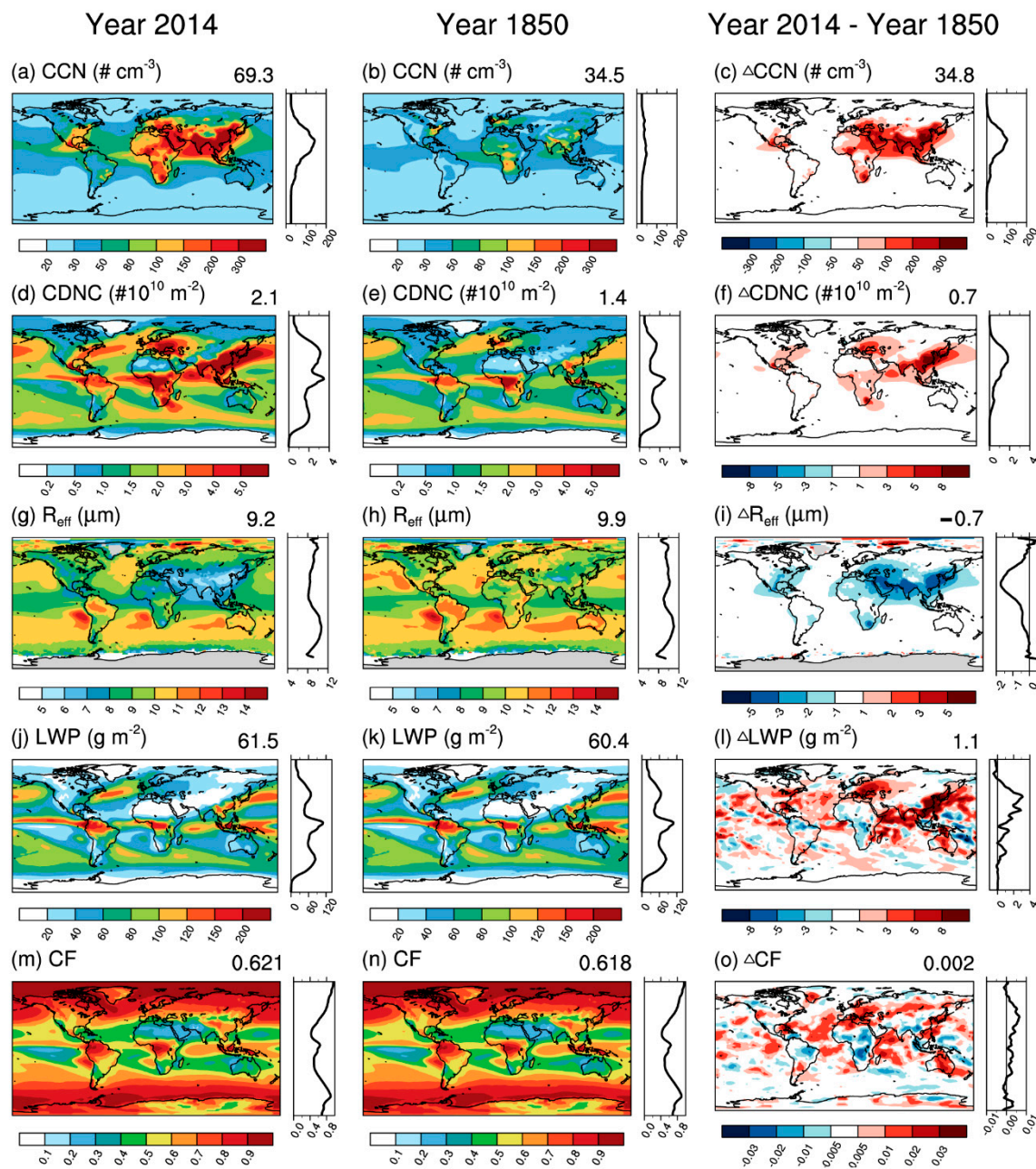

Figure 3. The modelled annual mean cloud physics properties in the year 2014 (left), the year 1850 (middle), and the years 2014–1850 (right). The zonal means plot is located in the right of each subplot. The global mean value is shown the top right corner of each map. The first row (**a–c**) is the cloud condensation nuclei (CCN) number concentration at a fixed 0.1% supersaturation at the surface in the model; the second row (**d–f**) is the column-integrated cloud droplet number concentration (CDNC); the third row (**g–i**) is the cloud droplet effective radius at the cloud top above the temperature of 273 K (R_{eff}); the fourth row (**j–l**) is the cloud liquid water path (LWP); and the last row (**m–o**) is the total cloud fraction (CF).

3.2.2. Aerosol–Cloud Interactions

The cloud, which accounts for about 67% of the Earth surface, can scatter lots of the solar radiation directly, exerting a strong "cooling effect" in the climate system. Assuming that anthropogenic aerosol

only contributes by the fine-mode sizes (those smaller than 1 μm) and that only indirect effect through low altitude water clouds matter. Therefore, only shortwave radiative effects are discussed here; for climate implications, longwave effects are ignored. Figure 4 shows the diagnosis results of the shortwave ERFaci between CAS-FGOALS-f3-L and the other five CMIP6 models results. Generally, the increase in anthropogenic aerosols causes an increase in the cloud droplets number concentration and the cloud lifetime, leading to a higher cloud albedo and consequent negative radiation forcing. The distributions of shortwave ERFaci in CAS-FGOALS-f3-L, which are consistent with that of the other five available CMIP6 models, are closely associated with changes in column-integrated cloud droplet number concentration (CDNC), cloud drop effective radius, liquid water path (LWP), and cloud fraction (CF). The strong negative radiation forcing areas mainly locate in the East Asia, South Asia, Europe, and their downwind regions. The global mean values of CRF_{SW} are −0.74, −0.59, 0.77, −2.45, and −1.02 W m^{-2} for CNRM-CM6-1, CNRM-ESM2-1, GFDL-ESM4, MRI-ESM2-0 and UKESM1-0-LL, respectively.
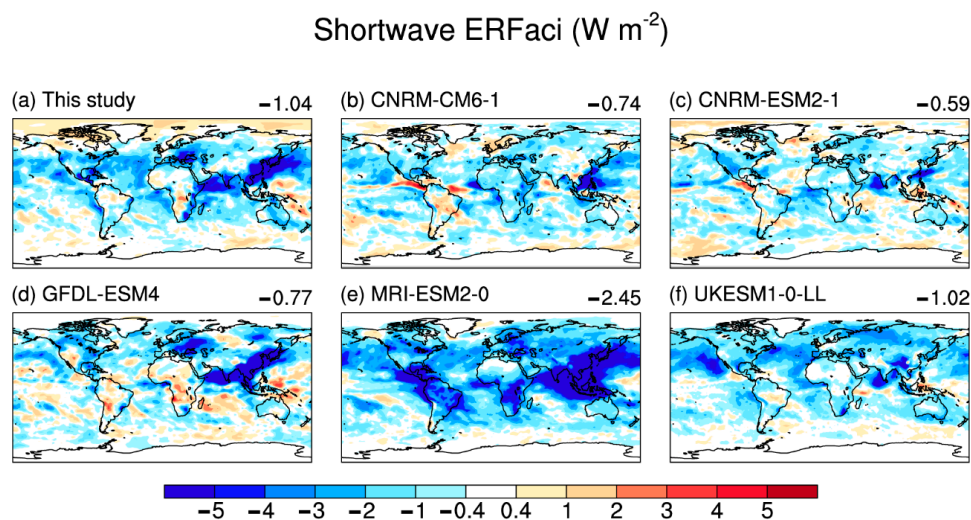
Figure 4. Comparison of annual mean shortwave effective radiative forcing of aerosol-cloud interactions in this study (**a**) and the five available (**b–f**) CMIP6 model results.

For the ice-cloud shortwave ERFaci, a Twomey-like effect may increase the albedo of ice cloud in the previous studies [50], whereas a strong variation in the response of ice cloud amount to aerosol still exist in the models, leaving the overall magnitude of the forcing uncertain [51]. In this study, the MRI-ESM2-0 model shows the strongest negative shortwave ERFaci (−2.45 W m^{-2}), which may be partly attributed to it allows the interaction between aerosols and ice clouds [52]. Therefore, the ERFaci in MRI-ESM2-0 is excluded in statistical calculations (Table 1). In sum, the assessing shortwave ERFaci in CAS-FGOALS-f3-L (−1.04 W m^{-2}) is slightly stronger than the multi-model average value from these CMIP6 models (−0.78 W m^{-2}), with a small standard deviation (0.18) (Table 1). The large diversities still exist in the local area, such as East Asia, South Asia, and Europe (Figure 4), implying that the interaction between aerosols and clouds still needs to further research to reduce this uncertainty.

3.3. Effective Radiative Forcing

Figure 5 shows the comparison of shortwave effective radiative forcing between CAS-FGOALS-f3-L and other 14 CMIP6 model results. The distributions of ERF_{SW} in CAS-FGOALS-f3-L are comparable with other 14 model results (except BCC-ESM1). The strong negative radiation forcing areas mainly locate in East Asia South Asia, Europe, and their downwind regions, which are similar to the distributions of shortwave ERFaci, implying that the ERF_{SW} are dominated by the shortwave ERFaci. Excluding the outlier among these models (i.e., BCC-ESM1), the modeled global mean ERF_{SW} value (−1.36 W m^{-2}) is slightly stronger than the multi-model average value from CMIP6 models

(-1.07 W m^{-2}) (Table 1), illustrating that the new coupled model can reproduce the aerosol radiation effect reasonably. The BCC-ESM1 model shows the strongest negative ERF$_{SW}$ (-3.9 W m^{-2}), possibly due in part to it uses a simple empirical function to represent the aerosol active process [53], which is more than five times larger relative to the minimum (GFDL-ESM4, -0.59 W m^{-2}) value of ERF$_{SW}$ among CMIP6 models, implying that the diversity in CMIP6 models still large. In addition, it is interesting that CAS-FGOALS-f3-L and MIROC6 applying the same SPRINTARS aerosol module, have a similar pattern but the ERF$_{SW}$ in CAS-FGOALS-f3-L (-1.36 W m^{-2}) is slightly weaker than that of MIROC6 (-1.61 W m^{-2}) (Figure 5a,m), which is possibly caused by the difference of carrier model. In order to maintain completeness of Formula (5), we also list the three components of the shortwave and longwave ERF (Table 1). The longwave ERF ($+0.2$ W m^{-2}) in AR5 is based on expert judgement, whereas Heyn et al. 2017 [10] found that the ERF in the terrestrial spectrum may be smaller in CMIP5 models. In this study, the assessing longwave ERF in CAS-FGOALS-f3-L is $+0.09$ W m^{-2}, which is slightly smaller than the CMIP6 multimodel means ($+0.12$ W m^{-2}) and the AR5 results. In addition, it can be seen that the ERF is mainly dominated by the ERFaci, the ERFari second, and the SRF is the smallest. The ERFaci in CAS-FGOALS-f3-L is -1.1 W m^{-2}, which is slightly stronger relative to the previous observation-based studies (-1.0 to -0.2 W m^{-2}) [51]. It is not clear that whether the observation-based estimates are more reliable with their own sources of uncertainty [51]. For the overall uncertainty in ERF, Bellouin et al. [54] recently provided a complete estimate in ERF (-2.0 to -0.35 W m^{-2}) with a 90% likelihood based on models, theory, and observations. The ERF in CAS-FGOALS-f3-L (-1.27 W m^{-2}) is in their estimate ranges, however, the model results may be better agree due to offsetting errors or because of same critical possibly false. The uncertainty of the ERF is still large, especially for the ERFaci.

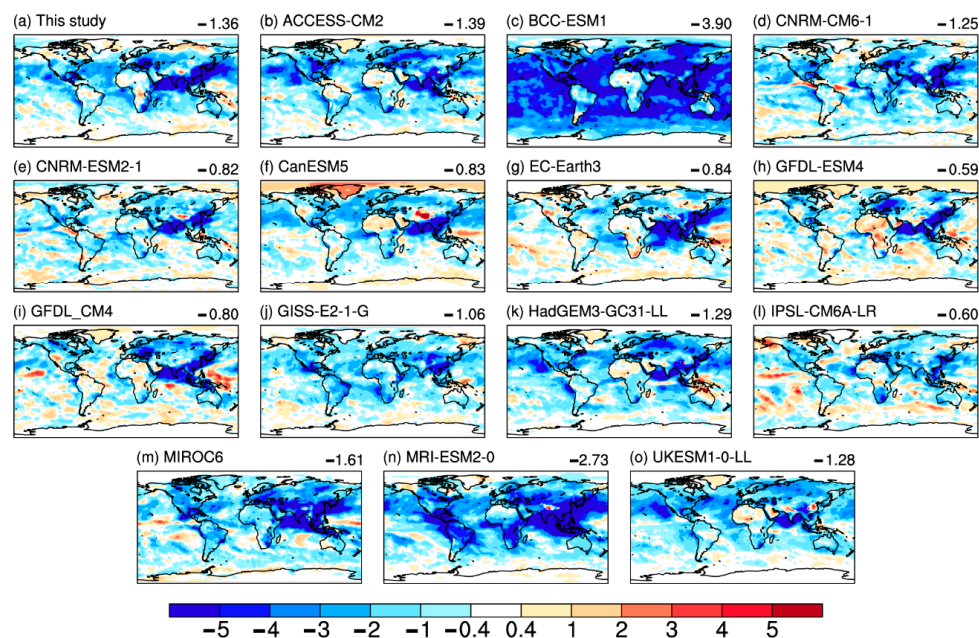## Shortwave effective radiative forcing (ERF$_{SW}$, W m^{-2})

Figure 5. Comparison of annual mean shortwave effective radiative forcing in this study (**a**) and the 14 available (**b**–**o**) CMIP6 model results.

4. Discussion

The CAS-FGOALS-f3-L can only reproduce direct aerosols radiation effect offline and missing the interactions between aerosols and cloud in the previous version. In this paper, we incorporate the aerosol-cloud interaction into the Chinese Academy of Sciences Flexible Global

Ocean–Atmosphere–Land System (CAS-FGOALS-f3-L) by coupling an existing aerosol module named Spectral Radiation Transport Model for Aerosol Species (SPRINTARS), which can more realistically represent the climate impacts of aerosols. A pronounced feature is that the atmospheric component named version 2 of the Finite-volume Atmospheric Model (FAMIL2) can perform a higher resolution aerosol simulation with the updated dynamic core to reproduce the microphysical processes at smaller scales and study the aerosol transportation in the complex terrain areas, such as the Tibet Plateau. The aerosol-radiation interaction and the aerosol-cloud interaction have been preliminary realized in our model, giving a chance to study the aerosol climate effect. Although the global mean and distribution of aerosol direct radiative forcing, cloud radiative forcing, and effective radiative forcing are comparable to other models in CMIP6, the challenges still exist.

On the one hand, it is definitely clear that the two moments aerosol and cloud parameterized scheme (i.e., mass and number concentration of aerosol particles and cloud drops are both predicted), can be more realistically to character the aerosol-cloud interaction [55]. Currently, however, the aerosol module SPRINTARS and CAS-FGOALS-f3-L atmospheric component FAMIL2 are still using the single moment scheme to predict the mass concentration and diagnosis the number concentration with pre-prescribed size distribution, this may hamper us to further dig out the important key factors related to aerosol-cloud interaction and bring a large uncertainty to assess the aerosol effective radiative forcing. Therefore, a two moments aerosol and cloud parameterized scheme are urgently required to be incorporated into the CAS-FGOALS-f3-L in the further.

On the other hand, as we know that the dust and black carbon particles can act as the ice nucleus to modify the properties of high cloud, however, the aerosol-cloud interaction in CAS-FGOALS-f3-L only considers the large scale warm stratus cloud, the aerosol-ice cloud and aerosol-mixed phase cloud interaction are both missing in the model. It is known that the second organic aerosol (SOA) contribute to a large portion in fine-mode aerosols, and the nitrate aerosols may important in local areas. These missing hygroscopic growth species can also participate the formation of cloud, perturbing the Earth's energy balance. In addition, the ERF also highly depends on the specific aerosol active scheme and cloud-rain autoconversion scheme, which related to the aerosol indirect effect. Therefore, exploring and refining these processes in future will allow us more precisely quantize how climate system "feel" the aerosol perturbation.

5. Conclusions

In this paper, we realize the aerosol–cloud interaction by incorporating the ARG (Abdul-Razzak and Ghan, [42]) aerosol activation scheme and the berry-type autoconversion scheme [43,44] into the CAS-FGOALS-f3-L which has participated the CMIP6, and further assess the effective radiation forcing (ERF) of anthropogenic aerosols and its decomposed components produced by the new coupled model CAS-FGOALS-f3-L based on the protocol of current CMIP6. The estimated ERF values and their spatial distributions are compared with the CMIP6 multi-model results. The main findings are summarized as follows:

(1) The total AOD in the year 2014 (global mean, 0.111) increases about 39% (0.031) relative to the year 1850 (global mean, 0.08), mainly due to the increase of anthropogenic aerosols. The sulfate and the carbonaceous aerosol contribute to about 71% (0.022) and 29% (0.009).

(2) The global mean 2014–1850 shortwave effective radiative forcing of aerosol-radiation interactions (ERFari) produced by CAS-FGOALS-f3-L (-0.27 W m^{-2}) is close to the multimodel mean value from 4 available CMIP6 models (-0.29 W m^{-2}). The pattern of the shortwave ERFari in CAS-FGOALS-f3-L are comparable with other models except the GFDL-ESM4. The GFDL-ESM4 model shows the strongest positive shortwave ERFari (+0.24 W m^{-2}), mainly due to its warming effect of absorbing black carbon is stronger than the cooling effect of scattering aerosols (i.e., sulfate and organic carbon).

(3) The global mean 2014–1850 shortwave effective radiative forcing of aerosol-cloud interactions (ERFaci) produced by CAS-FGOALS-f3-L (-1.04 W m^{-2}) is slightly stronger than the multi-model

mean value from the four available CMIP6 models (-0.78 W m^{-2}). The spatial distribution of the shortwave ERFaci in CAS-FGOALS-f3-L are consistent with the other four model results. The shortwave ERFaci is closely associated with changes in column-integrated cloud droplet number concentration (CDNC), cloud drop effective radius, liquid water path (LWP), and cloud fraction (CF). The MRI-ESM2-0 model shows the strongest negative shortwave ERFaci (-2.45 W m^{-2}), which may be partly attributed to being coupled to the aerosols-ice cloud interaction [52].

(4) The global mean 2014–1850 shortwave effective radiative forcing (ERF$_{SW}$) produced by CAS-FGOALS-f3-L (-1.36 W m^{-2}) shows a stronger negative forcing relative to the multi-model mean value from 11 available CMIP6 models (-1.07 W m^{-2}), and the pattern are also comparable, illustrating that the new coupled model can reasonably reproduce the aerosol radiation effect. The ERF is mainly dominated by the ERFaci, and the uncertainty of the ERF is still large, especially for the ERFaci.

These results provide an important reference to study the aerosol climate effect with the new coupling system and necessitate model improvements in some key processes, such as a two-moments aerosol and cloud microphysical scheme, adding SOA and nitrate aerosol, and explicitly character aerosol–ice cloud interaction, to better quantify the climate impacts of aerosols.

Supplementary Materials: The following are available online at http://www.mdpi.com/2073-4433/11/10/1115/s1, Figure S1: The changes of single scatter albedo in CAS-FGOALS-f3-L, Figure S2: The changes of precipitation in CAS-FGOALS-f3-L, Figure S3: The changes of High, Medium and Low Cloud Fraction in CAS-FGOALS-f3-L.

References

1. Haywood, J.; Boucher, O. Estimates of the direct and indirect radiative forcing due to tropospheric aerosols: A review. *Rev. Geophys.* **2000**, *38*, 513–543. [CrossRef]

2. Rosenfeld, D.; Andreae, M.O.; Asmi, A.; Chin, M.; de Leeuw, G.; Donovan, D.P.; Kahn, R.; Kinne, S.; Kivekäs, N.; Kulmala, M.; et al. Global observations of aerosol-cloud-precipitation-climate interactions. *Rev. Geophys.* **2014**, *52*, 750–808. [CrossRef]

3. Twomey, S. Aerosols, clouds and radiation. *Atmos. Environ. Part A. Gen. Top.* **1991**, *25*, 2435–2442. [CrossRef]

4. Qian, Y.; Yasunari, T.J.; Doherty, S.J.; Flanner, M.G.; Lau, W.K.M.; Ming, J.; Wang, H.; Wang, M.; Warren, S.G.; Zhang, R. Light-absorbing particles in snow and ice: Measurement and modeling of climatic and hydrological impact. *Adv. Atmos. Sci.* **2015**, *32*, 64–91. [CrossRef]

5. Boucher, O.; Randall, D.; Artaxo, P.; Bretherton, C.; Feingold, G.; Forster, P.; Kerminen, V.-M.; Kondo, Y.; Liao, H.; Lohmann, U.; et al. Clouds and aerosols. In *Climate Change 2013: The Physical Science Basis. Contribution of Working Group I to the Fifth Assessment Report of the Intergovernmental Panel on Climate Change*; Cambridge University Press: Cambridge, UK; New York, NY, USA, 2013; pp. 571–657.

6. Myhre, G.; Shindell, D.; Bréon, F.-M.; Collins, W.; Fuglestvedt, J.; Huang, J.; Koch, D.; Lamarque, J.-F.; Lee, D.; Mendoza, B.; et al. Anthropogenic and Natural Radiative Forcing. In *Climate change 2013: The Physical Science*

Basis. Contribution of Working Group I to the Fifth Assessment Report of the Intergovernmental Panel on Climate Change; Cambridge University Press: Cambridge, UK; New York, NY, USA, 2013; pp. 659–740.

7. Forster, P.M.; Richardson, T.; Maycock, A.C.; Smith, C.J.; Samset, B.H.; Myhre, G.; Andrews, T.; Pincus, R.; Schulz, M. Recommendations for diagnosing effective radiative forcing from climate models for CMIP6. *J. Geophys. Res. Atmos.* **2016**, *121*, 12460–12475. [CrossRef]

8. Pincus, R.; Forster, P.M.; Stevens, B. The Radiative Forcing Model Intercomparison Project (RFMIP): Experimental protocol for CMIP6. *Geosci. Model Dev.* **2016**, *9*, 3447–3460. [CrossRef]

9. Carslaw, K.S.; Lee, L.A.; Reddington, C.L.; Pringle, K.J.; Rap, A.; Forster, P.M.; Mann, G.W.; Spracklen, D.V.; Woodhouse, M.T.; Regayre, L.A.; et al. Large contribution of natural aerosols to uncertainty in indirect forcing. *Nature* **2013**, *503*, 67–71. [CrossRef]

10. Heyn, I.; Block, K.; Mülmenstädt, J.; Gryspeerdt, E.; Kühne, P.; Salzmann, M.; Quaas, J. Assessment of simulated aerosol effective radiative forcings in the terrestrial spectrum. *Geophys. Res. Lett.* **2017**, *44*, 1001–1007. [CrossRef]

11. Collins, W.J.; Lamarque, J.F.; Schulz, M.; Boucher, O.; Eyring, V.; Hegglin, M.I.; Maycock, A.; Myhre, G.; Prather, M.; Shindell, D.; et al. AerChemMIP: Quantifying the effects of chemistry and aerosols in CMIP6. *Geosci. Model Dev.* **2017**, *10*, 585–607. [CrossRef]

12. Bao, Q.; Wu, X.; Li, J.; Wang, L.; He, B.; Wang, X.; Liu, Y.; Wu, G. Outlook for El Niño and the Indian Ocean Dipole in autumn-winter 2018–2019. *Chin. Sci. Bull.* **2019**, *64*, 73. [CrossRef]

13. He, B.; Bao, Q.; Wang, X.; Zhou, L.; Wu, X.; Liu, Y.; Wu, G.; Chen, K.; He, S.; Hu, W.; et al. CAS FGOALS-f3-L Model Datasets for CMIP6 Historical Atmospheric Model Intercomparison Project Simulation. *Adv. Atmos. Sci.* **2019**, *36*, 771–778. [CrossRef]

14. Li, J.; Bao, Q.; Liu, Y.; Wu, G.; Wang, L.; He, B.; Wang, X.; Li, J. Evaluation of FAMIL2 in Simulating the Climatology and Seasonal-to-Interannual Variability of Tropical Cyclone Characteristics. *J. Adv. Model. Earth Syst.* **2019**, *11*, 1117–1136. [CrossRef]

15. Zhou, L.; Bao, Q.; Liu, Y.; Wu, G.; Wang, W.-C.; Wang, X.; He, B.; Yu, H.; Li, J. Global energy and water balance: Characteristics from Finite-volume Atmospheric Model of the IAP/LASG (FAMIL1). *J. Adv. Model. Earth Syst.* **2015**, *7*, 1–20. [CrossRef]

16. Lin, S.-J. A "Vertically Lagrangian" Finite-Volume Dynamical Core for Global Models. *Mon. Weather Rev.* **2004**, *132*, 2293–2307. [CrossRef]

17. Putman, W.M.; Lin, S.-J. Finite-volume transport on various cubed-sphere grids. *J. Comput. Phys.* **2007**, *227*, 55–78. [CrossRef]

18. Lamarque, J.-F.; Emmons, L.; Hess, P.; Kinnison, D.; Tilmes, S.; Vitt, F.; Heald, C.; Holland, E.; Lauritzen, P.; Neu, J.; et al. CAM-chem: Description and evaluation of interactive atmospheric chemistry in the Community Earth System Model. *Geosci. Model Dev.* **2012**, *5*, 369–411. [CrossRef]

19. Takemura, T.; Okamoto, H.; Maruyama, Y.; Numaguti, A.; Higurashi, A.; Nakajima, T. Global three-dimensional simulation of aerosol optical thickness distribution of various origins. *J. Geophys. Res. Atmos.* **2000**, *105*, 17853–17874. [CrossRef]

20. Takemura, T.; Nakajima, T.; Dubovik, O.; Holben, B.N.; Kinne, S. Single-scattering albedo and radiative forcing of various aerosol species with a global three-dimensional model. *J. Clim.* **2002**, *15*, 333–352. [CrossRef]

21. Takemura, T. Simulation of climate response to aerosol direct and indirects with aerosol transport-radiation model. *J. Geophys. Res. Atmos.* **2005**, *110*. [CrossRef]

22. Takemura, T.; Egashira, M.; Matsuzawa, K.; Ichijo, H.; O'ishi, R.; Abe-Ouchi, A. A simulation of the global distribution and radiative forcing of soil dust aerosols at the Last Glacial Maximum. *Atmos. Chem. Phys.* **2009**, *9*, 3061–3073. [CrossRef]

23. Wang, H.; Dai, T.; Daisuke, G.; Bao, Q.; He, B.; Liu, Y.; Takemura, T.; Nakajima, T.; Shi, G. Simulating and Evaluating the Global Aerosol Distributions with the Online Aerosol Coupled CAS-FGOALS Model. *J. Geophys. Res. Atmos.*. (under review).

24. Bao, Q.; Wu, G.; Liu, Y.; Yang, J.; Wang, Z.; Zhou, T. An introduction to the coupled model FGOALS1.1-s and its performance in East Asia. *Adv. Atmos. Sci.* **2010**, *27*, 1131–1142. [CrossRef]

25. Bao, Q.; Lin, P.; Zhou, T.; Liu, Y.; Yu, Y.; Wu, G.; He, B.; He, J.; Li, L.; Li, J.; et al. The Flexible Global Ocean-Atmosphere-Land system model, Spectral Version 2: FGOALS-s2. *Adv. Atmos. Sci.* **2013**, *30*, 561–576. [CrossRef]

26. Wu, G.; Hui, L.; Yucheng, Z.; Li, W. A Nine-layer Atmospheric General Circulation Model and Its Performance. *Adv. Atmos. Sci.* **1996**, *13*, 1–18.

27. Li, J.-X.; Bao, Q.; Liu, Y.-M.; Wu, G.-X. Evaluation of the computational performance of the finite-volume atmospheric model of the IAP/LASG (FAMIL) on a high-performance computer. *Atmos. Ocean. Sci. Lett.* **2017**, *10*, 329–336. [CrossRef]

28. Zhou, L.; Liu, Y.; Bao, Q.; Yu, H.; Wu, G. Computational Performance of the High-Resolution Atmospheric Model FAMIL. *Atmos. Ocean. Sci. Lett.* **2012**, *5*, 355–359.

29. Bretherton, C.S.; Park, S. A New Moist Turbulence Parameterization in the Community Atmosphere Model. *J. Clim.* **2009**, *22*, 3422–3448. [CrossRef]

30. Clough, S.; Shephard, M.; Mlawer, E.J.; Delamere, J.S.; Iacono, M.J.; Cady-Pereira, K.; Boukabara, S.A.; Brown, P. Atmospheric radiative transfer modeling: A summary of the AER codes. *J. Quant. Spectrosc. Radiat. Transf.* **2005**, *91*, 233–244. [CrossRef]

31. Harris, L.M.; Lin, S.-J. Global-to-Regional Nested Grid Climate Simulations in the GFDL High Resolution Atmospheric Model. *J. Clim.* **2014**, *27*, 4890–4910. [CrossRef]

32. Lin, Y.-L.; Farley, R.D.; Orville, H.D. Bulk Parameterization of the Snow Field in a Cloud Model. *J. Clim. Appl. Meteorol.* **1983**, *22*, 1065–1092. [CrossRef]

33. Zhou, L.; Lin, S.-J.; Chen, J.-H.; Harris, L.M.; Chen, X.; Rees, S.L. Toward Convective-Scale Prediction within the Next Generation Global Prediction System. *Bull. Am. Meteorol. Soc.* **2019**, *100*, 1225–1243. [CrossRef]

34. Xu, K.-M.; Randall, D.A. A Semiempirical Cloudiness Parameterization for Use in Climate Models. *J. Atmos. Sci.* **1996**, *53*, 3084–3102. [CrossRef]

35. Oleson, K.W.; Lawrence, D.M.; Gordon, B.; Flanner, M.G.; Kluzek, E.; Peter, J.; Levis, S.; Swenson, S.C.; Thornton, E.; Feddema, J. *Technical Description of Version 4.0 of the Community Land Model (CLM)*; NCAR Technical Note NCAR/TN-478+STR; National Center for Atmospheric Research: Boulder, CO, USA, 2010; p. 173.

36. Hunke, E.C.; Lipscomb, W.H.; Turner, A.K.; Jeffery, N.; Elliott, S. *CICE: The Los Alamos Sea Ice Model Documentation and Software User's Manual Version 4.1*; Tech. Rep LA-CC-06-012; T-3 Fluid Dynamics Group: Los Alamos, NM, USA, 2010; p. 675.

37. Goto, D.; Nakajima, T.; Takemura, T.; Sudo, K. A study of uncertainties in the sulfate distribution and its adiative forcing associated with sulfur chemistry in a global aerosol model. *Atmos. Chem. Phys.* **2011**, *11*, 10889–11091. [CrossRef]

38. Dai, T.; Goto, D.; Schutgens, N.A.J.; Dong, X.; Shi, G.; Nakajima, T. Simulated aerosol key optical properties over global scale using an aerosol transport model coupled with a new type of dynamic core. *Atmos. Environ.* **2014**, *82*, 71–82. [CrossRef]

39. Dai, T.; Cheng, Y.; Zhang, P.; Shi, G.; Sekiguchi, M.; Suzuki, K.; Goto, D.; Nakajima, T. Impacts of meteorological nudging on the global dust cycle simulated by NICAM coupled with an aerosol model. *Atmos. Environ.* **2018**, *190*, 99–115. [CrossRef]

40. Hoesly, R.; Smith, S.; Feng, L.; Klimont, Z.; Janssens-Maenhout, G.; Pitkanen, T.; Seibert, J.; Vu, L.; Andres, R.; Bolt, R.; et al. Historical (1750–2014) anthropogenic emissions of reactive gases and aerosols from the Community Emissions Data System (CEDS). *Geosci. Model Dev.* **2018**, *11*, 369–408. [CrossRef]

41. van Marle, M.J.E.; Kloster, S.; Magi, B.I.; Marlon, J.R.; Daniau, A.L.; Field, R.D.; Arneth, A.; Forrest, M.; Hantson, S.; Kehrwald, N.M.; et al. Historic global biomass burning emissions for CMIP6 (BB4CMIP) based on merging satellite observations with proxies and fire models (1750–2015). *Geosci. Model Dev.* **2017**, *10*, 3329–3357. [CrossRef]

42. Abdul-Razzak, H.; Ghan, S.J. A parameterization of aerosol activation: 2. Multiple aerosol types. *J. Geophys. Res. Atmos.* **2000**, *105*, 6837–6844. [CrossRef]

43. Berry, E.X. *Modification of the Warm Rain Process, 1st National Conference on Weather Modification*; American Meteorology Society: New York, NY, USA, 1968; pp. 81–85.

44. Sato, Y.; Goto, D.; Michibata, T.; Suzuki, K.; Takemura, T.; Tomita, H.; Nakajima, T. Aerosol effects on cloud water amounts were successfully simulated by a global cloud-system resolving model. *Nat. Commun.* **2018**, *9*, 985. [CrossRef]

45. Ghan, S.J. Technical Note: Estimating aerosol effects on cloud radiative forcing. *Atmos. Chem. Phys.* **2013**, *13*, 9971–9974. [CrossRef]

46. Grandey, B.S.; Rothenberg, D.; Avramov, A.; Jin, Q.; Lee, H.-H.; Liu, X.; Lu, Z.; Albani, S.; Wang, C. Effective radiative forcing in the aerosol–climate model CAM5.3-MARC-ARG. *Atmos. Chem. Phys.* **2018**, *18*, 15783–15810. [CrossRef]

47. Miller, R.L.; Perlwitz, J.; Tegen, I. Feedback upon dust emission by dust radiative forcing through the planetary boundary layer. *J. Geophys. Res. Atmos.* **2004**, *109*, D24209. [CrossRef]

48. Rothenberg, D.; Wang, C. An aerosol activation metamodel of v1.2.0 of the pyrcel cloud parcel model: Development and offline assessment for use in an aerosol–climate model. *Geosci. Model Dev.* **2017**, *10*, 1817–1833. [CrossRef]

49. Liu, X.; Easter, R.C.; Ghan, S.J.; Zaveri, R.; Rasch, P.; Shi, X.; Lamarque, J.F.; Gettelman, A.; Morrison, H.; Vitt, F.; et al. Toward a minimal representation of aerosols in climate models: Description and evaluation in the Community Atmosphere Model CAM5. *Geosci. Model Dev.* **2012**, *5*, 709–739. [CrossRef]

50. Gryspeerdt, E.; Sourdeval, O.; Quaas, J.; Delanoë, J.; Krämer, M.; Kühne, P. Ice crystal number concentration estimates from lidar–radar satellite remote sensing—Part 2: Controls on the ice crystal number concentration. *Atmos. Chem. Phys.* **2018**, *18*, 14351–14370. [CrossRef]

51. Gryspeerdt, E.; Muelmenstadt, J.; Gettelman, A.; Malavelle, F.F.; Morrison, H.; Neubauer, D.; Partridge, D.G.; Stier, P.; Takemura, T.; Wang, H.; et al. Surprising similarities in model and observational aerosol radiative forcing estimates. *Atmos. Chem. Phys.* **2020**, *20*, 613–623. [CrossRef]

52. Zelinka, M.D.; Andrews, T.; Forster, P.M.; Taylor, K.E. Quantifying components of aerosol-cloud-radiation interactions in climate models. *J. Geophys. Res-Atmos.* **2014**, *119*, 7599–7615. [CrossRef]

53. Wu, T.; Zhang, F.; Zhang, J.; Jie, W.; Zhang, Y.; Wu, F.; Li, L.; Yan, J.; Liu, X.; Lu, X.; et al. Beijing Climate Center Earth System Model version 1 (BCC-ESM1): Model description and evaluation of aerosol simulations. *Geosci. Model Dev.* **2020**, *13*, 977–1005. [CrossRef]

54. Bellouin, N.; Quaas, J.; Gryspeerdt, E.; Kinne, S.; Stier, P.; Watson-Parris, D.; Boucher, O.; Carslaw, K.S.; Christensen, M.; Daniau, A.L.; et al. Bounding Global Aerosol Radiative Forcing of Climate Change. *Rev. Geophys.* **2020**, *58*, e2019RG000660. [CrossRef] [PubMed]

55. Mann, G.W.; Carslaw, K.S.; Reddington, C.L.; Pringle, K.J.; Schulz, M.; Asmi, A.; Spracklen, D.V.; Ridley, D.A.; Woodhouse, M.T.; Lee, L.A.; et al. Intercomparison and evaluation of global aerosol microphysical properties among AeroCom models of a range of complexity. *Atmos. Chem. Phys.* **2014**, *14*, 4679–4713. [CrossRef]